RSC Advances

PAPER

View Article Online
View Journal | View Issue

Cite this: *RSC Adv.*, 2025, **15**, 35312

Catalytic hydroconversion of Shaerhu subbituminous coal over an Ni-based MOF-derived carbon matrix superacid catalyst

Li Li,[a] Yu-Fan Ren,[a] Chang-Wang Shao,[b] Long-Yu Zhang,*[ac] Xian-Yong Wei *[d] and Xing-Shun Cong*[a]

A magnetic solid acid, TFMSA/CNOFW, was prepared by impregnating trifluoromethanesulfonic acid (TFMSA) into a calcined nickel–organic framework (CNOFW) at room temperature. The extraction residue (ER) of Shaerhu subbituminous coal (SSBC) obtained by ultrasonic extraction with an isometric carbon disulfide/acetone mixed solvent was subjected to non-catalytic hydroconversion (NCHC) and catalytic hydroconversion (CHC) over the TFMSA/CNOFW in *n*-hexane at 300 °C for 4 h. The soluble portions from NCHC (SP_{NCHC}) and CHC (SP_{CHC}) were analyzed using a gas chromatograph/mass spectrometer. Results suggest that, compared with SP_{NCHC}, the introduction of the TFMSA/CNOFW dramatically improved the yield of SP_{CHC} (from 14.1% to 35.8%). Furthermore, arenes and oxygen-containing compounds were predominant in SP_{CHC} without cyclanes, indicating that the TFMSA/CNOFW efficiently promoted the cleavage of the >CH–O– bridge bonds in SSBC without hydrogenation of aromatic rings. The TFMSA/CNOFW can facilitate the transfer of mobile H^+ from heterolytic H_2 to the oxygen atom on the >CH–O– bridged bonds in SSBC or the substituents of the aromatic rings connected by bridge chains, leading to breakage of the bridged bonds. Such a mechanism was demonstrated by the CHC of 2-(benzyloxy)naphthalene.

Received 7th August 2025
Accepted 12th September 2025

DOI: 10.1039/d5ra05772h

rsc.li/rsc-advances

1. Introduction

Subbituminous coals are abundant fossil resources. Nevertheless, their characteristically low calorific value and elevated organic oxygen content render them inherently inadequate for direct combustion.[1–4] Structurally, these coals comprise cross-linked macromolecular matrices featuring abundant oxygen-functionalized bridged linkages (*e.g.*, >C–O–, –OH, and –COOH). Many soluble organic compounds, especially arenes and oxygen-containing organic compounds (OCOCs), can be released by the cleavage of these bridged linkages, which can be considered raw materials for value-added chemicals and clean liquid fuels.[5–7] Therefore, understanding the structural characteristics of the molecular composition and directed conversion mechanism of subbituminous coal is crucial for developing non-fuel utilization technology.

Direct coal liquefaction (DCL) is an available option for converting coal directly into soluble portions and value-added chemicals.[8,9] At the same time, high temperature and hydrogen pressure make DCL economically inefficient, which increases the generation of gaseous products and coke. Catalytic hydroconversion of subbituminous coals offers opportunities to obtain a high yield of soluble portions owing to the fact that the probe catalyst can mitigate harsh reaction conditions and enhance DCL efficiency. Both catalysts and active hydrogen species play important roles in this process. Previous studies have indicated that noble metal catalysts (*e.g.*, Pd, Ru, and Pt) exhibit exceptional activity in the catalytic hydrogenation of aromatic rings (ARs). However, their industrial application is limited by prohibitive costs and carbon deposition. In comparison, non-noble metal catalysts, particularly nickel-based catalysts, have been favored as promising non-noble metal catalysts for their high degree of hydrodeoxygenation and cost-effectiveness. Solid acids have received great attention from researchers because of their relatively high catalytic activity, low corrosivity, and eco-friendly properties. A survey of the literature revealed that solid acid catalysts effectively promote coal depolymerization to afford soluble components with relatively high yields.[10,11] Furthermore, solid acids have exhibited high activity in the hydrocracking of subbituminous coal extraction residue.[12] Hence, it is meaningful to study the

[a]*College of Chemistry, Chemical Engineering and Material Science, Zaozhuang University, Zaozhuang 277160, Shandong, China*
[b]*Shandong Goldencell Electronics Technology Co., Ltd, Zaozhuang 277800, Shandong, China*
[c]*State Key Laboratory of Heavy Oil Processing, College of Chemical Engineering, China University of Petroleum (East China), Qingdao, 266580, Shandong, China*
[d]*Yili Key Laboratory of Chemistry and Chemical Engineering on Heavy Carbon Resources, Yili Normal University, Yining 835000, Xinjiang, China*

catalytic hydrocracking of SSBC for producing soluble fractions over nickel-based solid acid catalysts.

Solid superacids have drawn the attention of many researchers for their ability to catalyze the cleavage of the bridged bonds in coal more efficiently under mild conditions.[13,14] Although conventional solid acids, such as zeolites, amberlyst, and other supported acids, are widely used in catalytic conversion, they are often limited by insufficient acid, the complexity of the products and inefficient catalyst recovery. To overcome these limitations, trifluoromethanesulfonic acid (TFMSA), a strong organic acid, can be impregnated into a suitable support, such as activated carbon, attapulgite powder, zirconia, or zeolite 5A, to prepare a high-activity, solid super-acid catalyst.[15–18] The calcined nickel–organic framework (CNOFW), which was prepared by the pyrolysis of a nickel–organic framework (NOFW) as a support, would be superior to the abovementioned supports due to Ni's ability to enhance the adsorption of the benzene ring onto the substrate. The free H^+ released from TFMSA plays an essential role in the cleavage of the bridge bonds and side-chains in middle- and low-ranked coal, significantly increasing their yield of soluble portions. This catalytic structure combines exceptional acidity with the practical advantages of magnetic separation, enabling the selective cleavage of the >C–O bridge bonds within the macromolecular structure of the low-rank coal. This unique design offers a tailored platform for facilitating the conversion of aromatics.

The stability and reusability of catalysts play a crucial role in determining their practical utility. Doping strategies have been demonstrated as effective approaches for enhancing the stability of catalysts.[19–21] Herein, TFMSA/CNOFW was prepared *via* the impregnation of TFMSA into CNOFW and subsequently employed for the CHC of ER from SSBC. In comparison to other solid acid catalysts, TFMSA/CNOFW can be efficiently separated under the influence of an external magnetic field. This characteristic is of paramount importance for the catalyst's reusability. A comparative analysis of the yields and molecular compositions of the soluble products obtained from NCHC and CHC over TFMSA/CNOFW was conducted.

2. Experimental

The detailed preparation of the catalysts and their characterization are described in the SI.

3. Results and discussion

3.1. Catalyst characterization

The thermogravimetric (TG) analysis of NOFW (Fig. 1) revealed a 10.1% mass loss within the range of 30 to 175 °C, corresponding to both the evaporation of physically adsorbed water (surface and pore-confined) and the decarboxylation of carboxyl groups. This is a physical process; thus, NOFW could still maintain its structure. In addition, the weight loss between 175 and 265 °C mainly resulted from the vaporization of coordinated water and the adsorbed DMF guest molecules in the pores. The maximum mass loss between 370 and 450 °C is primarily owing to the collapse of the NOFW structure accompanied by the decomposition of organic ligands, resulting in a mass loss of 39.4%.[22] The mass loss plateaued above 450 °C, confirming the thermal stability of the nickel-coated carbon material post-calcination. Based on the results of the TG analysis, four calcination temperatures (400 °C, 500 °C, 600 °C, and 700 °C) were selected to systematically evaluate the effect of the pyrolysis temperature on the catalytic performance.

As exhibited in Fig. 2a and b, NOFW and CNOFW-*T* exhibit microporous–mesoporous composite structures. Compared with NOFW, the SSA of CNOFW-*T* decreased because the precursor of the NOFW skeleton structure gradually collapsed. With increasing pyrolysis temperature, the SSA of CNOFW increased, indicating that a high pyrolysis temperature is favorable for forming new pores.[23] However, when the temperature increased to 700 °C, the SSA decreased sharply due to sintering of the CNOFW. Interestingly, CNOFW-600 possesses the most enormous SSA and pore volume (Table S2). Furthermore, CNOFW-600 has a lower adsorption capacity and a more obvious hysteresis loop, indicating that it has more mesopores than CNOFW, which may be due to the overall dimensional shrinkage of CNOFW and the solidification properties of the carbonized products.[24] Impregnating TFMSA into CNOFW decreased the SSA from 145.1 to 97.8 $m^2 g^{-1}$, but significantly enlarged the APD from 1.5 nm to 3.1 nm, further suggesting a strong corrosive effect on CNOFW. In addition, TFMSA/CNOFW exhibits micropore and mesopore bimodal structures based on its pore size distributions. Among them, the tiny pores serve as anchoring sites for the nickel nanoparticles (NNPs). In contrast, the large pore network facilitates hydrocracking of

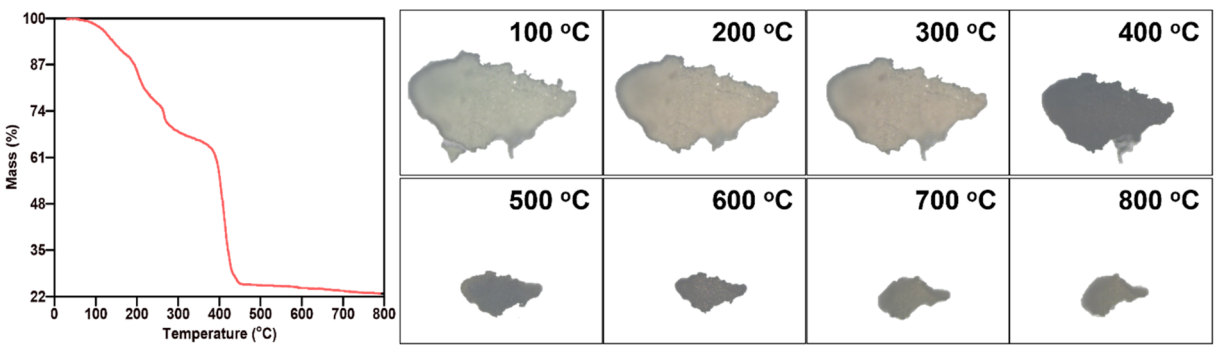

Fig. 1 TG and high-temperature hot-stage microscopy of the NOFW.

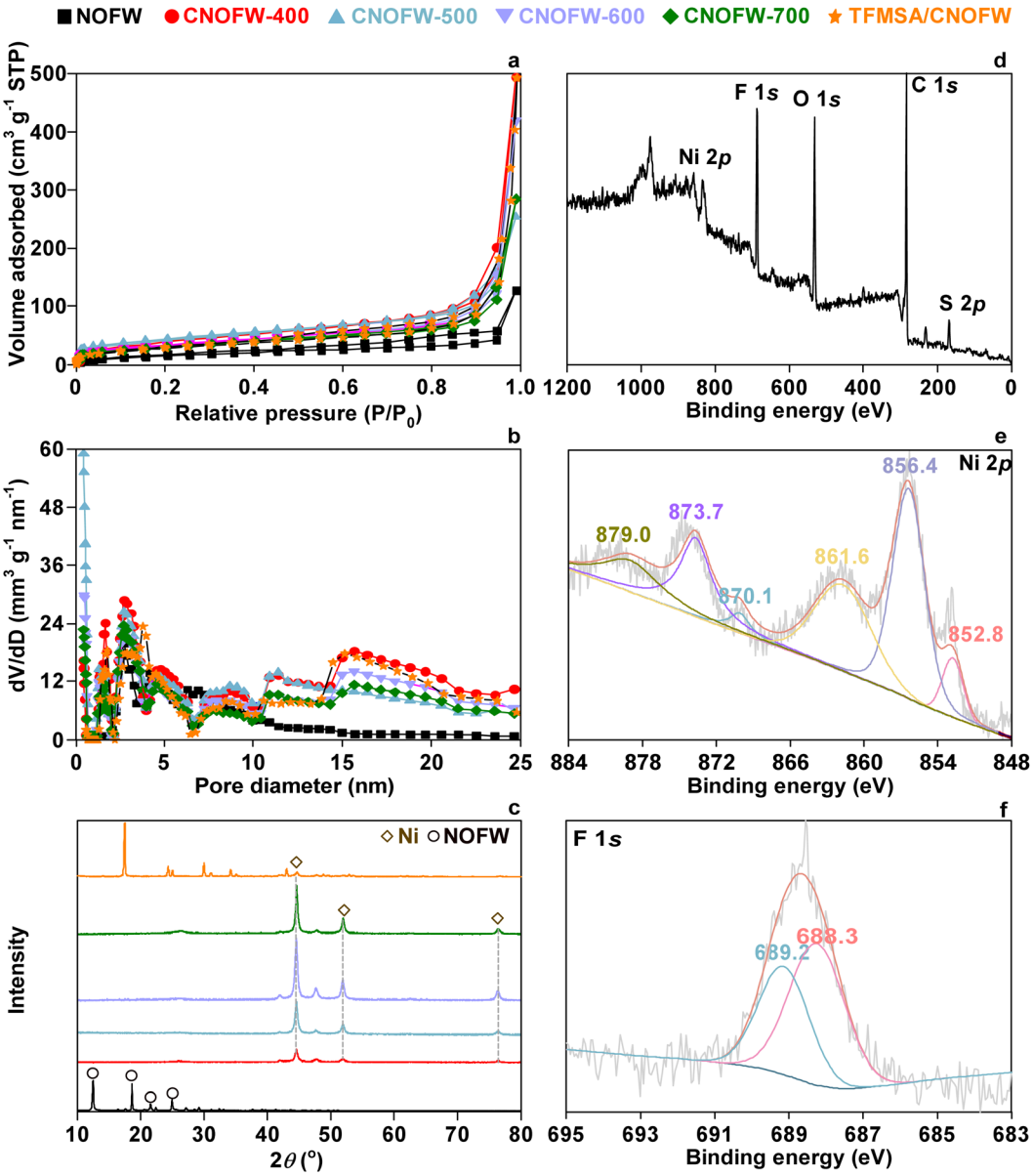

Fig. 2 (a) N_2 adsorption/desorption isotherms, (b) pore size distribution curves and (c) XRD patterns of the samples, (d–f) XPS of the TFMSA/CNOFW.

macromolecules and enables rapid diffusion of reactants and products, thereby enhancing the catalyst's activity.[25]

As displayed in Fig. 2c, the pronounced characteristic diffraction peaks (CDPs) of NOFW can be well indexed to the previous literature,[26] indicating that NOFW was well-developed and successfully prepared. Compared with NOFW, all the CDPs in CNOFW-*T* are different from those in NOFW, suggesting complete collapse of the NOFW skeleton during calcination and the formation of Ni nanoparticles with a face-centered cubic crystal structure. Notably, the crystallinity increased with increasing pyrolysis temperature, suggesting that elevated temperatures promote the growth of the NNPs. The CDPs of around 17.2°, attributed to TFMSA, confirm the loading of TFMSA onto CNOFW. Moreover, TFMSA disrupted the ordering of the crystal structures, resulting in weakening of the crystal structure of CNOFW.

Fig. S1 and Table S3 illustrate the elements, Ni, C, and O on the surface of CNOFW-*T*. With increasing pyrolysis temperature, the atomic abundance of Ni increased and reached its maximum (3.9%) at 600 °C. As shown in Fig. 2d–f, the Ni 2p and F 1s associated peaks appear to be around 848–884 eV and 695–683 eV, respectively, according to XPS. The atomic abundance of the elements Ni, F, C, S and O on the surface of TFMSA/CNOFW is 3.5, 3.4, 79.0, 4.9 and 9.2%, respectively (Table S4). In the spectrum of Ni $2p_{3/2}$, the binding energy of 852.8 eV corresponds to Ni^0, while the peaks at 856.4 eV and 873.7 eV were assigned to Ni^{2+} species, consistent with the facile oxidation of Ni upon exposure to air. From Fig. 2f, the O 1s peaks with the

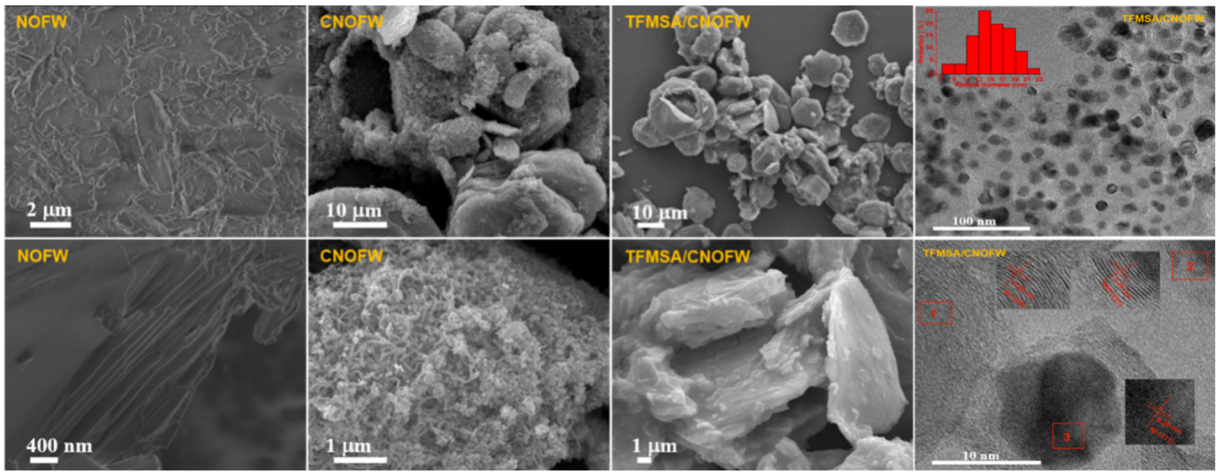

Fig. 3 SEM images of the samples.

binding energies of 688.3 and 689.2 eV confirmed the existence of the F–C and F–O bonds.[27] These results further confirmed the successful loading of TFMSA onto the CNOFW surface, indicating a strong interfacial interaction between the two components.

As shown in Fig. 3, the light-green, powdered NOFW exhibits a sheet-like structure with a smooth surface, while CNOFW shows a vesicular structure with pancake-like stacking and a fluffy, rough and fibrous texture. The metal–organic skeleton structure collapsed during the high calcination temperatures, and the active metal components were confined inside the fibrous structure, which hindered the aggregation of the NNPs. After loading TFMSA, the approximately hexagonal structure remained unchanged, and the fiber-like aggregates on the surface disappeared in favor of folds. The NNPs and the exposed surface crystal facets of the catalyst were further confirmed by HRTEM. The NNPs were evenly dispersed on the surface of CNOFW, with an average diameter between 13 and 17 nm without apparent aggregation. Furthermore, noticeable lattice fringes attributed to Ni and NiO were also clearly observed in HRTEM.

As Fig. 4 illustrates that the magnetization curve of TFMSA/CNOFW exhibits a characteristic hysteresis loop that passes through the central origin, demonstrating its superparamagnetic behavior with negligible remanence and coercivity.[28] The saturation magnetization of TFMSA/CNOFW decreased to 10.6 emu g^{-1} compared with that of CNOFW (34.4 emu g^{-1}). Although the magnetic properties decreased, the magnetic catalyst was still able to achieve rapid separation with the reaction substrate by applying an external magnetic field.

Fig. 5a illustrates that there are free acidic sites on the surface of CNOFW and four distinct NH_3 desorption peaks at 160.3 °C, 269.5 °C, 465.4 °C, and 640.1 °C that were assigned to weak, middle, and strong acid sites in TFMSA/CNOFW. The introduction of TFMSA produced strong acid sites, resulting in higher activity for donating mobile H^+.[29] As shown in Fig. 5b, the bands around 1455 cm^{-1} and 1540 cm^{-1} are attributed to

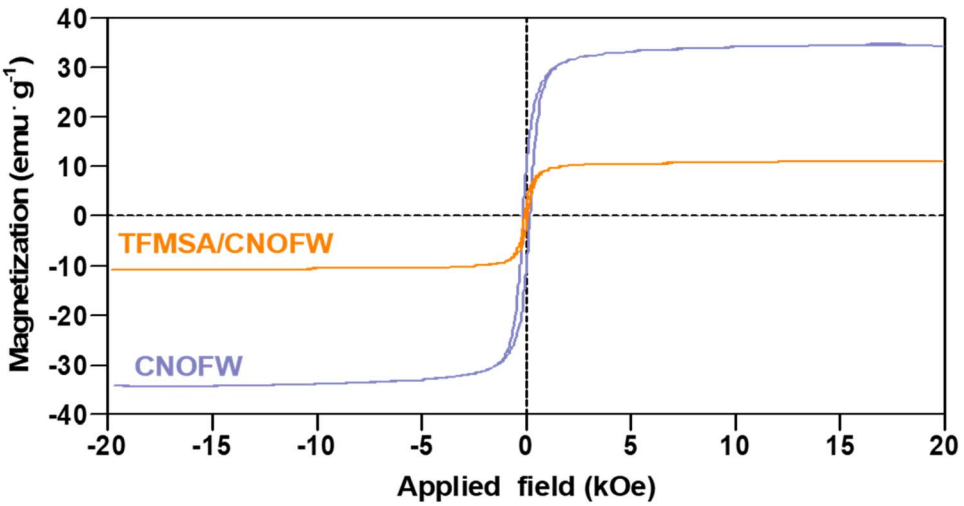

Fig. 4 Magnetic hysteresis loops of the samples.

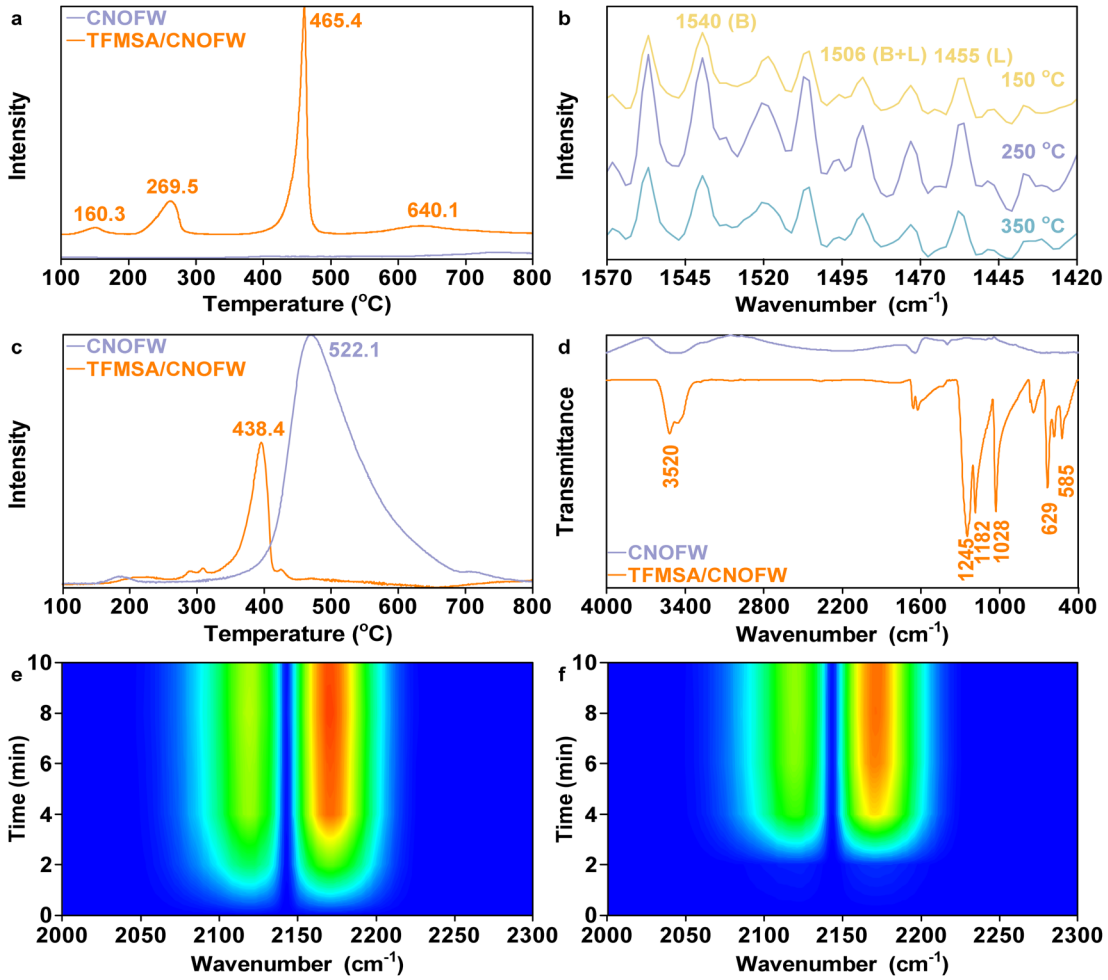

Fig. 5 (a) TPD of NH_3, (b) PyIR spectra, (c)TPR of H_2 and (d) FTIR spectra of the CNOFW and TFMSA/CNOFW. *In situ* DRIFTS of (e) the TFMSA/CNOFW and (f) CNOFW adsorption of CO at 35 °C.

pyridine adsorbed onto the Lewis and Brønsted acid sites, respectively, whereas the band at 1490 cm^{-1} was attributable to the combined contribution of both acidic species.[30] These results further confirmed that TFMSA was successfully loaded onto CNOFW.

Fig. 5c demonstrates that there is a H_2 consumption peak around 522.1 °C in CNOFW, which is ascribed to the reduction of the bulk Ni^{2+} species with a strong interaction with the carbon matrix. In comparison, the narrow peak around 438.4 °C in TFMSA/CNOFW is attributed to the reduction of the products formed by the interaction of the Ni^{2+} species and TFMSA. After loading TFMSA, the interaction between CNOFW and NiO was weakened due to the interaction of particulate NiO with TFMSA, resulting in a shift of the reduction peak to a low temperature. As shown in Fig. 5d, the characteristic peak around 3520 cm^{-1} is assigned to the stretching vibration of the –OH group. Only four characteristic peaks appeared in TFMSA/CNOFW. Among these peaks, the prominent characteristic peaks observed around 1245 and 1182 cm^{-1} likely correspond to the symmetric and asymmetric stretching vibrations of the S=O bond, respectively. In comparison, the stretching vibrations attributed to the C–F and C–S bonds were observed around 1028 and 629 cm^{-1}, respectively. Furthermore, the peak observed at 585 cm^{-1} corresponds to the Ni–O stretching vibration.[31] These results further imply that TFMSA was successfully loaded into CNOFW, and there is an interaction between CNOFW and TFMSA.

Fig. 5e and f clearly illustrates that TFMSA/CNOFW exhibits a preferential adsorption of O atoms. This phenomenon can be attributed to the enhanced acidity resulting from the addition of TFMSA. Furthermore, the strong adsorption of the O atoms is advantageous as it helps to suppress their over-hydrogenation.

3.2. CHC of 2-(benzyloxy)naphthalene (BON) under different conditions

The catalytic hydrogenolysis of BON has often been investigated in connection with coal because this molecule is representative of other components in coal. BON was employed as a coal-related model compound to investigate the mechanism of the CHC of ER from SSBC. As shown in Fig. 6, under a IHP of 1 MPa for 90 min, the conversion of BON as well as the selectivities for toluene and naphthalen-2-ol increased with rising reaction temperature; thus, 160 °C was considered as the optimal reaction temperature. At 160 °C under 1 MPa for 90 min, BON was

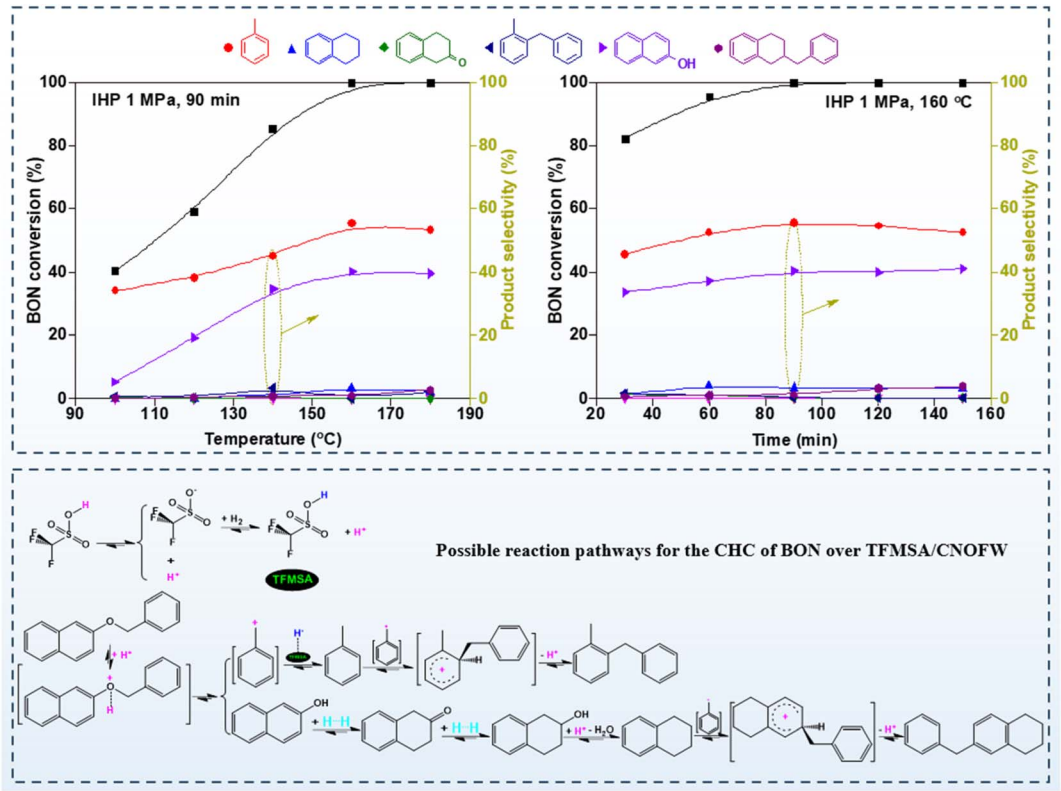

Fig. 6 CHC of BON under different conditions and possible pathways.

completely converted, with a combined selectivity for toluene and naphthalen-2-ol reaching 95.8%. This result further demonstrates the high catalytic activity of TFMSA/CNOFW for >C–O– hydrogenolysis under mild conditions. Notably, the high BON conversion depended on H^+ over TFMSA/CNOFW. Furthermore, the activity of TFMSA/CNOFW was investigated for the hydrocracking of other CRMCs containing the >C–O– bridge bond. As shown in Table S2, TFMSA/CNOFW also exhibited excellent catalytic hydrocracking activity for POB and OBMDB under mild conditions.

As Fig. 6 demonstrates, TFMSA/CNOFW was able to heterogeneously split H···H obtained from the activated H_2 into mobile H^+ and catalyst surface-immobilized H^-. The mobile H^+ preferentially attacked the electronegative oxygen atom in BON, forming protonated BON. The benzyl cation, produced by hydrocracking of protonated BON, was further combined with H^- fixed on the surface of TFMSA/CNOFW to yield toluene, as the primary reaction. The trace side-reactions proceed in the following ways: (I) 1-benzyl-2-methylbenzene was generated *via* attack of toluene by the benzyl cation; (II) tetraline was

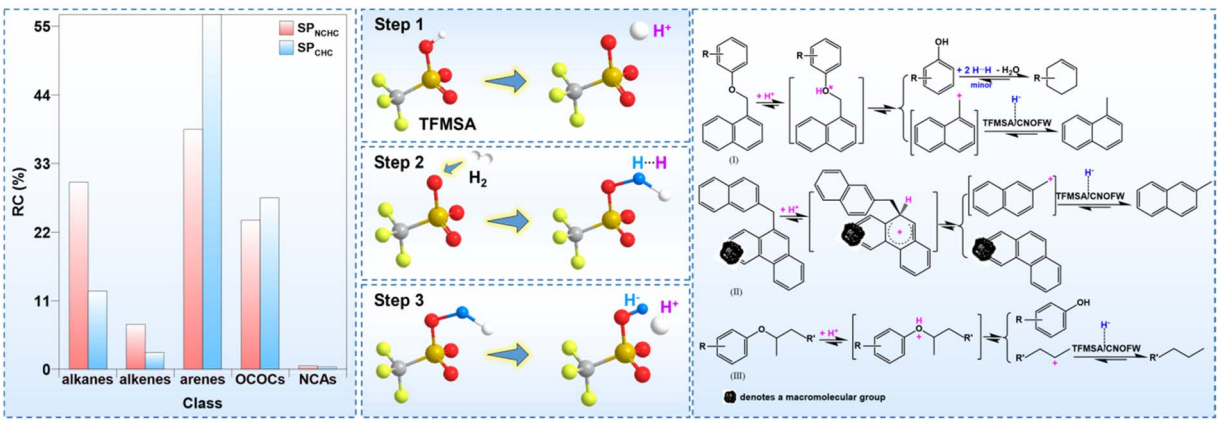

Fig. 7 Distributions of different classes in SP_{NCHC} and SP_{CHC} according to the analysis using GC/MS and possible pathways for the formation of MN and alkylphenol from the CHC of ER over TFMSA/CNOFW.

generated from naphthalen-2-ol due to the synergistic effect of H···H; and H^+ transfer at the benzyl cation formed 6-benzyl-1,2,3,4-tetraline.

3.3. CHC of SP

Understanding the differences in the structure and composition of the soluble portions obtained from NCHC and CHC can provide crucial information on the structure of coal macromolecules. The yield of SP_{CHC} (35.8%) significantly exceeded that of SP_{NCHC} (14.1%), indicating that TFMSA/CNOFW can dramatically promote the hydrogenolysis of ER, resulting in more soluble organic small molecules. Comprehensive chromatographic analysis (Fig. S3 and S4) identified 214 distinct organic compounds in SP_{NCHC} and SP_{CHC}, which were systematically categorized into alkanes, alkenes, arenes, nitrogen-containing aromatics (NCAs), and OCOCs, as listed in

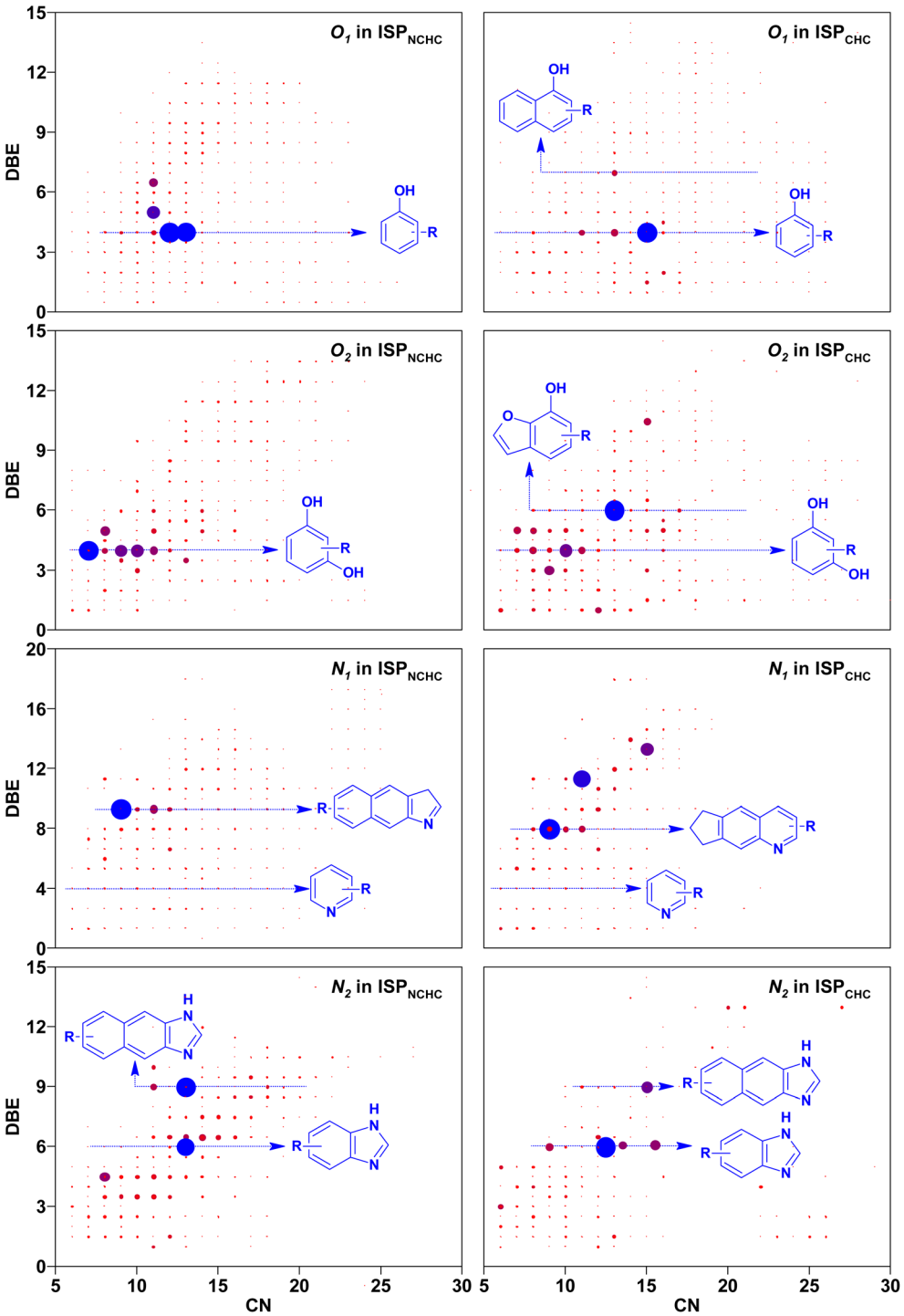

Fig. 8 Iso-abundance plots of DBE *vs.* CN for *N* and *O* class species in ISP_{NCHC} and ISP_{CHC} according to the analysis using QPEOTMS.

Tables S6–S38, respectively. All the alkanes except 2,6-dimethylundecane, 2,6,10-trimethyldodecane, and 3-methyltetradecane are normal alkanes. As Fig. S5 and 7 display, arenes are dominant in both SP_{NCHC} and SP_{CHC}, while OCOCs have significantly higher relative contents (RCs) in SP_{CHC} than in SP_{NCHC}. The generation of OCOCs from NCHC originated from the thermal dissociation of the strong hydrogen bonds in ER. In contrast, the substantial quantity of OCOCs detected in SP_{CHC} was likely generated from the catalytic cleavage of the >C–O– bonds in ER. Noteworthily, cyclanes were not detected in SP_{NCHC} and SP_{CHC}, indicating that TFMSA/CNOFW exhibited excellent activity for the catalytic hydrocracking of ER rather than hydrogenation, which is informative for the catalytic hydrocracking of low- and middle-ranked coals to obtain platform compounds. Compared with SP_{NCHC}, there was a substantial increase in terms of the species and content of arenes in SP_{CHC}, especially for the compounds with a high degree of condensation, *e.g.*, containing 4–5 rings, suggesting that TFMSA/CNOFW promoted the depolymerization of ER leading to more arenes in SP_{CHC}. Interestingly, chain alkenes were only detected in SP_{NCHC}, but not in SP_{CHC} due to the cleavage of the >C=C< bond in ER promoted by TFMSA/CNOFW. Notably, the enylarenes detected in SP_{CHC} suggest that the available hydrogen was preferentially utilized for cleaving the >C–O bonds and stabilizing the resulting reactive fragments, rather than for saturating the aromatic rings or alkyl side chains.

As demonstrated in Fig. 7, the F_3CSO_3 moiety with a strong electron-withdrawing ability facilitated the formation of mobile H^+ and $F_3CSO_2O^-$/CNOFW was immobilized on the support, which subsequently reacted with exogenous hydrogen to generate mobile H^+ and immobile H^- attached to the TFMSA/CNOFW surface. The generated H^+ served as a catalytic species, facilitating the selective cleavage of the >C–O bond through electrophilic activation. The possible pathway for the CHC of ER was explored by using alkylphenols and methylnaphthalene, which had high yields in SP_{CHC}. For compounds containing the >C–O– bridge bonds, H^+ preferentially occurred at the electronegative oxygen atom in compounds **I** or **III**, forming a protonated intermediate. This intermediate subsequently underwent heterolytic cleavage of the $>C_{alk}$–O– bridge bond, yielding an alkylphenol (phenols with the highest yields in the hydrocracked products of SSBC) and naphthalenemethyl or alkyl positive ions, which then combined with H^- adhered to TFMSA/CNOFW to generate methylnaphthalene or alkanes. For compounds containing the >C–C bonds, extensive research has been conducted on the solid acid-catalyzed transformation of di(1-naphthyl)methane under temperature-controlled conditions,[32] and it was proposed that the hydrocracking reaction was attributable to the H^+ reaction mechanism. The carbon atom with the largest superdissociation energy in compound **II** was preferentially attacked by H^+ leading to $>C_{ar}$–C_{alk} cleavage to produce methylnaphthalenes and arenes linked to large molecular groups. In summary, the strong acidity of the TFMSA/CNOFW facilitated the free availability of H^+ from heterolytic H_2; this H^+ was either transferred to the oxygen atoms on the bridge bonds in ER or to the substituents of the aromatic rings connected by the bridge chains, leading to the breakage of the bridge bonds.

As displayed in Fig. 8 and S2, more species of small molecular compounds were enriched in SP_{CHC} compared to SP_{NCHC}, indicating that the introduction of TFMSA/CNOFW promoted the depolymerization of organic macromolecules and enriched the number of organic species. Furthermore, the *O*1 class species in ISPs have a double bond equivalent (DBE) range of 6–20, indicating that the ISPs are rich in OCOCs with 1–2 aromatic rings, predominantly phenolic hydroxyl groups. According to the basic rules of the DBE calculation, each successive benzene ring incorporated into an aromatic structure contributes an incremental increase of 3 units to the overall DBE value.[33] The DBE values of 4 and 7 coupled with a carbon number (CN) range of 6–15 in the *O*1 class species were identified as belonging to alkylphenol and naphthol derivatives. In the *O*2 class, the DBE and CN values of the ISPs are concentrated in the range of 2–15 and 5–25, suggesting that OCOCs in the *O*2 class species contain 1 to 3 AR(s) with a varying length of the alkyl side chain substituents. It was inferred that the *O*2 class species detected in the ISPs with DBE values of 4, 7 and 10 are alkyl dihydroxy compounds with 1–3 ARs. For the NCAs, the compounds in the *N*1 class species can be attributed to alkylpyridines, quinolines and benzoquinolines, respectively. In the *N*2 class, due to the high conjugation effect of the condensed aromatic structures, the cleavage energy threshold increased with an increase in the number of aromatic ring. It was inferred that the *N*2 species with DBE values of 6 and 9 are alkylbenzimidazoles and naphthylimidazoles, respectively.

As shown in Fig. 9, the characteristic absorption band observed around 3450 cm^{-1} was assigned to the stretching vibration of the phenolic hydroxyl group in SPs. The absorption bands corresponding to -$>CH_3$ and $>CH_2$ stretching vibrations around 2923, 2850 and 1450 cm^{-1} in SP_{CHC} are both dramatically sharper than those in SP_{NCHC},[34] indicating an abundance of aliphatic structures in SP_{CHC}, which was due to the cleavage of the methylene bridge bond in ER over TFMSA/CNOFW. Moreover, the absorbances corresponding to the >C=O stretching vibration around 1705 cm^{-1} and the >C–O– vibration at approximately 1260 cm^{-1} in SP_{CHC} are also enhanced

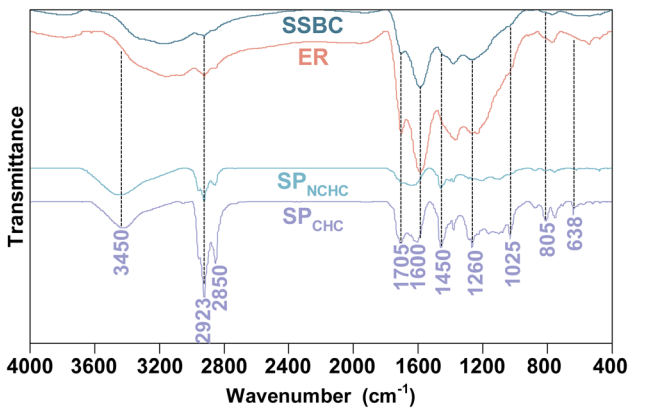

Fig. 9 FTIR spectra of the samples.

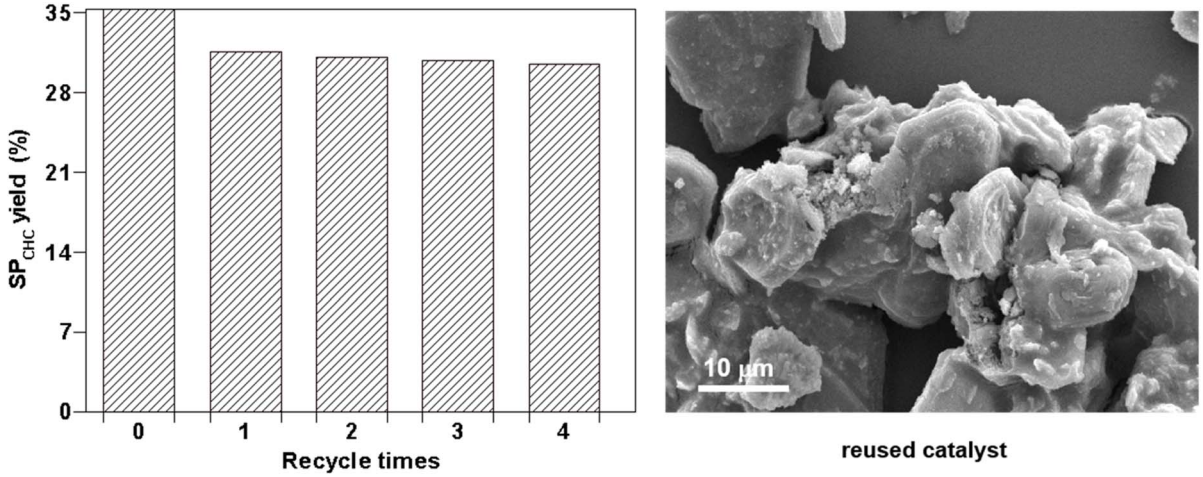

Fig. 10 Stability test of TFMSA/CNOFW and SEMI of the recycled TFMSA/CNOFW.

compared to SP_{NCHC}, suggesting an enrichment of OCOCs. The absorbances of the skeleton and the out-of-plane bending vibrations of the >C–H groups of ARs at approximately 1600 and 638 in the spectra obtained from SP_{CHC} were stronger than those observed in the spectra for SP_{NCHC}, indicating a higher concentration of arenes, specifically alkylnaphthalenes and dimethylnaphthalenes (Fig. S5). Additionally, a distinct absorption peak attributed to the Ar–OH stretching vibration around 1025 cm^{-1} was exclusively observed in SP_{CHC}. This observation is consistent with the higher relative content of OCOCs in SP_{CHC}, particularly alkylphenols and dimethylphenols, as displayed in Fig. 7. In contrast, the characteristic band associated with the >C–O–C< bridged bond around 1230 cm^{-1} almost disappeared. These findings further confirm that the cleavage of the >C–O–C< bond in ER occurred in CHC.

3.4. Reusability of TFMSA/CNOFW from the CHC of ER

The reusability of TFMSA/CNOFW was evaluated by the CHC of ER under similar conditions (1 g ER, 0.2 g recycled TFMSA/CNOFW, 1 MPa of IHP, 300 °C and 4 h). As depicted in Fig. 10, TFMSA/CNOFW exhibited favorable reusability in terms of the yield of SP_{CHC}, *i.e.*, the yield of SP_{CHC} decreased significantly in the first run, which may be attributed to the leaching of the TFMSA acid site. However, it stabilized in the subsequent cycles and remained above 30%, which confirmed the excellent reusability of the catalyst. Moreover, the SEMI of the reused TFMSA/CNOFW showed slight agglomeration on its surface, which was responsible for the decrease in its activity.

4. Conclusion

The TFMSA/CNOFW composite was successfully synthesized through a modified impregnation approach. Comprehensive catalyst characterisations confirmed the successful incorporation of TFMSA onto the CNOFW surface, revealing a strong interfacial interaction between TFMSA and the CNOFW component. TFMSA/CNOFW was proven to be effective in activating H_2 and exhibited exceptional catalytic performance for the CHC of both ER and BON. At 160 °C under 1 MPa for 90 min, BON underwent a complete conversion, and the combined selectivity for toluene and naphthalen-2-ol was 95.8%. At 300 °C under 1 MPa for 4 h, the yield of SPCHC was 35.8%. The significantly enhanced yield of SP_{CHC} compared to SP_{NCHC} from ER can be primarily ascribed to the efficient proton release from TFMSA/CNOFW and subsequent proton transfer to the oxygen atom in the ER structure. In contrast to the hydrogenation reactions of other subbituminous coals, this particular process exhibited a low propensity for generating saturated cyclanes. Abundant aromatic groups and OCOCs were detected in SP_{NCHC} and SP_{CHC} without any cyclanes, indicating that the TFMSA/CNOFW efficiently promoted the cleavage of the >CH–O bridge bond in ER but not the cleavage of hydrogenated aromatic rings. In addition, this phenomenon aligns with the element transfer reaction theory,[35] suppresses the formation of cyclane by-products during the reaction, and contributes to the relatively simple composition of SP_{CHC}, which was conducive for obtaining pure organic compounds through subsequent separation, reducing the cost of product separation. This study provides some insights and strategies for the efficient and sustainable application of subbituminous coal in an industrial context.

Conflicts of interest

There are no conflicts of interest to declare.

Data availability

The data supporting this article have been included as part of the SI. Supplementary information is available. See DOI: **https://doi.org/10.1039/d5ra05772h**.

Acknowledgements

This work was financially supported by the National Natural Science Foundation of China (Grants 22478334 and 51674223)

and Natural Science Foundation of Shandong Province (Grants ZR2022MB027).

References

1 P. Chavarria, M. T. Martinez, J. L. Miranda and J. Osàcar, *Fuel Process. Technol.*, 1986, **13**(2), 205–211.
2 S. F. Yuan, N. Zhang, X. Qu, J. C. Bi, Q. Cao and J. L. Wang, *Fuel*, 2017, **200**, 153–161.
3 H. Liu, Z. H. Li, Y. L. Yang, G. D. Miao and Y. Z. Han, *Energy*, 2023, **272**, 127122.
4 W. C. Xia, C. K. Niu and C. C. Ren, *J. Cleaner Prod.*, 2017, **168**, 1032–1038.
5 Y. Gao, Y. Y. Tian, M. L. Hao, S. X. Li, L. Y. Sun and P. Liang, *J. Anal. Appl. Pyrolysis*, 2024, **179**, 106489.
6 Q. L. Qiu, D. P. Pan and F. Zeng, *Energy Sources, Part A*, 2024, **46**, 13459–13469.
7 S. Yan, J. C. Bi and X. Qu, *Appl. Energy*, 2017, **206**, 401–412.
8 W. Li, Z. Q. Bai, J. Bai and X. Li, *Fuel*, 2017, **197**, 209–216.
9 R. Gautam and R. Vinu, *React. Chem. Eng.*, 2020, **5**(8), 1320–1373.
10 H. F. Shui, X. Z. Chen, Z. C. Wang and D. X. Zhang, *Fuel*, 2010, **89**(1), 67–72.
11 H. Kumagai, Y. Sanada and N. Yoneda, *Fuel Process. Technol.*, 1986, **14**, 171–181.
12 Y. Y. Liu, K. Murata and M. Inaba, *Catal. Today*, 2019, **332**, 115–121.
13 Y. H. Huang, S. Q. Xia and P. S. Ma, *Catal. Commun.*, 2017, **89**, 111–116.
14 G. C. Jiang, Y. H. Hu, G. Q. Xu, X. D. Mu and H. Z. Liu, *ACS Sustainable Chem. Eng.*, 2018, **6**(5), 5772–5783.
15 C. E. J. J. Vriamont, T. Y. Chen, C. Romain, P. Corbett, P. Manageracharath, J. Peet, C. M. Conifer, J. P. Hallett and G. J. P. Britovsek, *ACS Catal.*, 2019, **9**(3), 2345–2354.
16 Z. R. Yan, Q. H. Liu, L. X. Liang and O. Y. Jing, *J. CO_2 Util.*, 2021, **47**, 101489.
17 M. S. Frei, C. Mondelli, A. Cesarini, F. Krumeich, R. Hauert, J. A. Stewart, D. C. Ferré and J. Pérez-Ramírez, *ACS Catal.*, 2020, **10**(2), 1133–1145.
18 M. Zhao, X. Wang, J. Xu, Y. Q. Li, X. M. Wang, X. Chu, K. Wang, Z. J. Wang, L. L. Zhang, J. Feng, S. Y. Song and H. J. Zhang, *Adv. Mater.*, 2024, **36**(21), 2313596.
19 Q. M. Fang, Q. H. Sun, R. X. Zhang, H. W. Wang and J. Qi, *Mater. Today Chem.*, 2025, **46**, 102770.
20 B. W, J. F. Zhang, J. T. Zhang, L. L. Li, N. D. Tan and Z. Chen, *J. Environ. Chem. Eng.*, 2025, **13**(5), 118259.
21 F. Y. Zhou, Q. Xin, Y. J. Fu, Z. S. Hua, Y. Dong, M. C. Ran, H. Song, S. J. Liu, R. Y. Qu, Y. Yang, X. Zhang, C. H. Zheng and X. Gao, *Chem. Eng. J.*, 2023, **464**, 142471.
22 S. S. Acharyya, S. Ghosh, S. Adak, T. Sasakib and R. Bal, *Catal. Sci. Technol.*, 2014, **4**, 4232–4241.
23 T. J. Liu, Z. T. Han, J. H. Jing, Q. L. Zeng, Y. Tian and D. Ma, *Energy Fuels*, 2024, **38**(21), 21277–21286.
24 L. J. Zhang, Z. X. Su, F. L. Jiang, L. L. Yang, J. J. Qian, Y. F. Zhou, W. M. Li and M. C. Hong, *Nanoscale*, 2014, **6**, 6590–6602.
25 L. Li, X. Y. Wei, G. H. Liu, Z. Li, J. H. Li, F. J. Liu, Q. Q. Kong, Z. C. Fan, Z. M. Zong and H. C. Bai, *Fuel*, 2022, **316**, 123185.
26 Q. M. Gao, H. N. He, K. M. Zhao, Z. He and S. Q. Liu, *J. Colloid Interface Sci.*, 2018, **530**, 127–136.
27 I. Niedermaier, N. Taccardi, P. Wasserscheid, F. Maier and H. P. Steinruck, *Angew. Chem., Int. Ed.*, 2013, **52**(34), 8904–8907.
28 Z. Y. Yan, X. F. Wang, Y. F. Zhang, Z. Y. Zhang, L. Qi, B. R. Miao and Q. B. Li, *Appl. Catal., B*, 2024, **358**, 124389.
29 S. P. Pati, B. Bhushan, A. Basumallick, S. Kumar and D. Das, *Mater. Sci. Eng., B*, 2011, **176**(13), 1015–1020.
30 L. Y. Zhang, L. Li, M. Li, Z. Q. Liu, X. Y. Wei, H. Ma and X. S. Cong, *J. Energy Inst.*, 2024, **117**, 101838.
31 A. Murad, J. Y. C. Liew, M. H. Yaacob, I. M. Noor, N. H. Osman, M. A. Kamarudin, S. T. Tan, H. K. Lee, Z. A. Talib, M. T. Alresheedi and M. A. Mahdi, *J. Phys. Chem. Solids*, 2022, **167**, 110743.
32 M. X. Zhao, X. Y. Wei, M. Qu, Z. K. Li, J. Liu, J. Kong, D. D. Zhang, H. L. Yan and Z. M. Zong, *Fuel Process. Technol.*, 2016, **142**, 258–263.
33 L. Hu, X. H. Guo, X. Y. Wei, F. J. Liu, M. L. Xu, T. L. Liu and F. B. Zhang, *Energy*, 2023, **279**, 128097.
34 H. F. Shui, J. T. Yao, H. H. Wu, Z. K. Li, J. C. Yan, Z. C. Wang, S. B. Ren, Z. P. Lei and C. C. Xu, *Fuel*, 2022, **315**, 123237.
35 H. G. Cao, X. R. Xiao, X. Zhang, Y. Y. Zhang and L. Yu, *Chin. Chem. Lett.*, 2025, **36**(9), 110924.